

Cite this: *Chem. Sci.*, 2025, 16, 18652

All publication charges for this article have been paid for by the Royal Society of Chemistry

# Engineered interface coverage and precise cocatalyst placement in MOF-derived heterojunction photocatalysts for selective methane oxidation

Wendi Zhao,<sup>†a</sup> Kang Sun,<sup>†a</sup> Jiayi Xu,<sup>a</sup> Zhongyuan Lin,<sup>a</sup> Qihui Chen,<sup>ID</sup><sup>\*b</sup> Maochun Hong,<sup>ID</sup><sup>b</sup> and Hai-Long Jiang,<sup>ID</sup><sup>\*a</sup>

While the rational fabrication of heterojunction photocatalysts with tunable interfaces and precise location control of cocatalysts holds great promise for enhanced photocatalysis, the synergistic integration of these parameters remains a substantial challenge. Herein, a series of metal–organic framework (MOF) composites with compact interfaces and customizable interface coverage are designed by epitaxial growth of ZIF-8 on the surface of MIL-125-NH<sub>2</sub>, yielding ZIF-8<sub>m</sub>/MIL-125-NH<sub>2</sub> ( $m = 21, 35, 65$ , representing the coverage percentage of ZIF-8 on the MIL-125-NH<sub>2</sub> surface). These composites are then converted into ZnO/TiO<sub>x</sub> heterojunctions through a two-step thermal treatment, termed ZTO- $m$ , for photocatalytic CH<sub>4</sub> oxidation. The results reveal that the interface coverage in ZTO- $m$  plays critical roles in charge separation, where ZTO-65 gives the best activity. With ZTO-65 as a basis, the cocatalysts, Au clusters and CoO<sub>x</sub> species, are respectively positioned onto TiO<sub>x</sub> and ZnO. The targeted positioning of cocatalysts not only improves charge separation but also facilitates O<sub>2</sub> activation. As a result, the resulting Au-Co-ZTO demonstrates excellent activity toward liquid oxygenate production, achieving 1723.5 μmol g<sup>-1</sup> h<sup>-1</sup> with a selectivity of 99%, in photocatalytic CH<sub>4</sub> oxidation.

Received 28th June 2025  
Accepted 4th September 2025

DOI: 10.1039/d5sc04771d

rsc.li/chemical-science

## Introduction

Matter transformation, the fundamental process underlying life activities, is an inherently energy-consuming process due to the thermodynamic limitation. The realization of efficient matter transformation under mild conditions represents a long-standing objective in scientific research. Photocatalysis, which harnesses light energy to drive chemical reactions, offers a promising way to overcome thermodynamic barriers and facilitate energy-intensive reactions under mild conditions.<sup>1–3</sup> To improve the photocatalytic performance, various strategies have been developed,<sup>4–11</sup> among which constructing heterojunctions and incorporating cocatalysts have emerged as very promising approaches.<sup>8–11</sup>

In heterojunction systems, interface interaction plays crucial roles in determining charge transfer efficiency.<sup>12</sup> However, challenges such as lattice mismatch and chemical incompatibility often prevent the formation of tightly bonded

heterojunction interfaces between different components.<sup>13</sup> As a result, heterojunction photocatalysts are typically constructed by simple physical assembly, which tends to result in poor interface contact and inefficient charge transfer. Achieving a tight, well-structured interface and precisely regulated interface area/length between two semiconductor photocatalysts remains a significant challenge. In addition, cocatalysts are widely recognized for enhancing charge separation and substrate activation in photocatalysis, while their random distribution often diminishes these advantages.<sup>14</sup> This limitation is particularly pronounced in heterojunction photocatalysts with complex components, where precise location control of cocatalysts becomes increasingly challenging. Therefore, the development of heterojunction systems with closely contacted interfaces and precisely positioned cocatalysts could significantly improve the photocatalytic efficiency. Unfortunately, such design has rarely been reported so far, and it remains a grand challenge to achieve using conventional methods.<sup>15,16</sup>

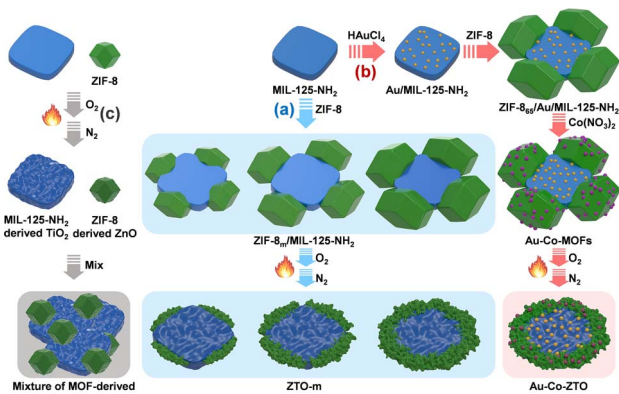
Metal–organic frameworks (MOFs), distinguished by their extraordinary structural versatility, have attracted widespread attention across diverse application fields.<sup>17–23</sup> MOFs exhibit high structural compatibility and customizable skeletons, enabling the fabrication of composites with controllable components, sizes, and interfaces.<sup>24–26</sup> Moreover, MOFs can

<sup>a</sup>Hefei National Research Center for Physical Sciences at the Microscale, Department of Chemistry, University of Science and Technology of China, Hefei, Anhui 230026, P. R. China. E-mail: jianglab@ustc.edu.cn; Web: <http://mof.ustc.edu.cn/>

<sup>b</sup>State Key Laboratory of Structural Chemistry, Fujian Institute of Research on the Structure of Matter, Chinese Academy of Sciences, Fuzhou, Fujian 350002, P. R. China. E-mail: chenqh@fjirm.ac.cn

<sup>†</sup> These authors contributed equally to this work.





**Scheme 1** Illustration showing the stepwise synthesis route to the fabrication of (a)  $ZTO-m$ , (b)  $Au-Co-ZTO$ , and (c) MOF-derived  $ZnO + TiO_2$  mixture photocatalysts for  $CH_4$  oxidation.

serve as versatile precursors for creating different derivatives tailored to diverse applications.<sup>27–30</sup> More importantly, these MOF-derived materials often inherit the original morphology and interface characteristics of their parent MOFs.<sup>31–33</sup> By leveraging the inherent tunability of MOFs, it might be possible to fabricate MOF-based composites with tunable interfaces and precise cocatalyst placement as precursors, followed by thermal treatment to afford heterojunction photocatalysts with inherited structural features for improved photocatalysis.

In this work, binary MOF composites with controlled interface coverage were obtained by controlling the epitaxial growth of ZIF-8 on the surface of MIL-125-NH<sub>2</sub>, affording ZIF-8<sub>*m*</sub>/MIL-125-NH<sub>2</sub> ( $m = 21, 35, 65$ , representing the coverage percentage of ZIF-8 on the MIL-125-NH<sub>2</sub> surface). Subsequently,  $ZTO-m$  composites featuring varying heterojunction interface coverages between zinc oxide (ZnO) and titanium oxide (TiO<sub>x</sub>) were synthesized *via* a two-step thermal treatment of ZIF-8<sub>*m*</sub>/MIL-125-NH<sub>2</sub> (Scheme 1a). The heterojunction interface area (with *m* as the descriptor; see SI, Discussion S1) is found to significantly influence charge separation, and as a result,  $ZTO-65$  affords optimal performance toward photocatalytic  $CH_4$  oxidation. Further, Au clusters and CoO<sub>x</sub> species, serving as cocatalysts, were loaded onto ZIF-8 and MIL-125-NH<sub>2</sub>, respectively, to form the Au-Co-MOF composite with a ZIF-8 coverage of 65%, followed by thermal treatment to yield  $Au-Co-ZTO$  (Scheme 1b). Results demonstrate that the cocatalyst distribution not only suppresses the recombination of electrons and holes but also plays a crucial role in O<sub>2</sub> activation. Remarkably, the optimized  $Au-Co-ZTO$ , featuring Au clusters on TiO<sub>x</sub> and CoO<sub>x</sub> on ZnO, achieves a production rate of 1723.5  $\mu\text{mol g}^{-1} \text{h}^{-1}$  with 99% selectivity toward liquid oxygenate production in photocatalytic  $CH_4$  oxidation.

## Results and discussion

### Synthesis and characterization

Initially, MIL-125-NH<sub>2</sub> was prepared with titanium isopropoxide and aminoterephthalate *via* a hydrothermal method at 150 °C. Subsequently, ZIF-8 was grown on the surface of MIL-125-NH<sub>2</sub>

particles *via* an epitaxial growth strategy.<sup>34</sup> By adjusting the amount of ZIF-8 precursor, the ZIF-8<sub>*m*</sub>/MIL-125-NH<sub>2</sub> composites ( $m$  indicates the coverage percentage of ZIF-8 on the surface of MIL-125-NH<sub>2</sub> particles,  $m = 21, 35, 65$ ) were obtained. Powder X-ray diffraction (XRD) shows that the intensity ratio of diffraction peaks for ZIF-8 and MIL-125-NH<sub>2</sub> reasonably increases with higher ZIF-8 loading (Fig. S1). Scanning electron microscopy (SEM) observation further confirms the different degrees of ZIF-8 coverage on the MIL-125-NH<sub>2</sub> surface (Fig. 1a and S2). The coverage percentage of ZIF-8 on the MIL-125-NH<sub>2</sub> surface is controlled from 21% to 35%, and up to 65% (Fig. S3). The limitation in coverage is attributed to the inherent growth restrictions of ZIF-8 on the periphery of MIL-125-NH<sub>2</sub>.<sup>34</sup>

The above ZIF-8<sub>65</sub>/MIL-125-NH<sub>2</sub> composites were transformed into  $ZTO-65$  *via* pyrolysis in O<sub>2</sub> at 425 °C, followed by N<sub>2</sub> treatment at 600 °C (Scheme 1a). The first pyrolysis under an oxygen atmosphere produced metal oxides. During this process, the original morphology of MIL-125-NH<sub>2</sub> is largely inherited in the resulting titanium oxide, while the external ZIF-8 is transformed into porous ZnO with a stacked structure, as previously reported.<sup>35</sup> Powder XRD profiles reveal that, while ZIF-8 and MIL-125-NH<sub>2</sub> are respectively converted to ZnO and TiO<sub>2</sub> upon thermal treatment, for ZIF-8<sub>65</sub>/MIL-125-NH<sub>2</sub>, only ZnO diffraction peaks can be observed, with the absence of TiO<sub>2</sub> signals (Fig. S4). This absence of crystalline TiO<sub>2</sub> might be attributed to the influence of Zn during pyrolysis, which inhibits the crystallization of TiO<sub>2</sub>, leading to the formation of amorphous TiO<sub>x</sub>.<sup>36</sup> To enhance the interface interaction, higher pyrolysis temperatures were investigated.<sup>37</sup> While temperatures above 500 °C promote the formation of tight ZnO/TiO<sub>x</sub> interfaces, too high temperature leads to structural collapse (Fig. S4 and S5). As a result of optimization, the ZIF-8<sub>65</sub>/MIL-125-NH<sub>2</sub> composite was first treated in an oxygen atmosphere at 425 °C to produce metal oxide products, followed by N<sub>2</sub> treatment at 600 °C. The inert N<sub>2</sub> atmosphere would facilitate compact interfacial contact and avoid structural collapse.<sup>38</sup> Such a two-step process yields  $ZTO-65$ , in which not only a well-structured

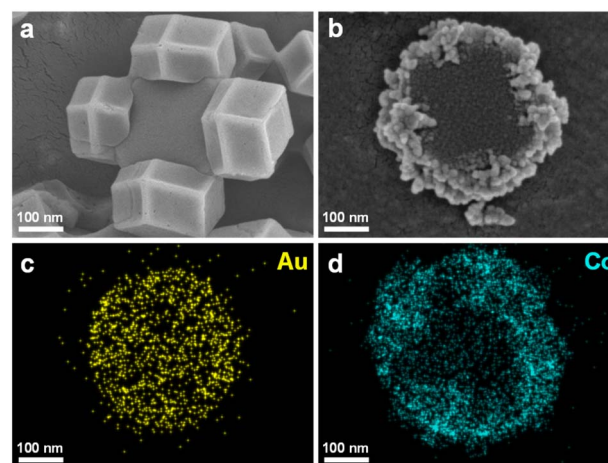


**Fig. 1** SEM images of (a) ZIF-8<sub>65</sub>/MIL-125-NH<sub>2</sub>, and (b)  $Au-Co-ZTO$ . (c) and (d) EDS mapping of Au and Co elements for  $Au-Co-ZTO$ .



heterojunction is maintained but also a new  $\text{Zn}_2\text{TiO}_4$  phase is created (Fig. S6 and S7).

The emergence of this new phase suggests a compact interface within the heterojunction, facilitating charge separation.<sup>39</sup> As verification, photocurrent and electrochemical impedance spectroscopy (EIS) results confirm that **ZTO-65** prepared *via* the two-step thermal treatment possesses superior charge separation compared to that produced by direct pyrolysis (Fig. S8). The results indicate that the two-step process not only largely preserves the morphology of the parent MOFs but also promotes the formation of a compact interface, improving charge separation. Additionally, **ZTO-21** and **ZTO-35**, with different coverage levels, were also prepared as controls under identical transformation conditions (Fig. S9 and S10).

Moreover, two cocatalysts, Au clusters and  $\text{CoO}_x$ , are introduced into the **ZTO** heterojunction system. The spatial arrangement of these cocatalysts is precisely controlled by varying the introduction sequence of cocatalyst precursors (Scheme 1b). Typically, Au clusters were first photodeposited on the surface of MIL-125-NH<sub>2</sub>, followed by the epitaxial growth of ZIF-8, during which the coverage percentage of ZIF-8 remained at the optimized value of 65%. Subsequently,  $\text{Zn}^{2+}$  within ZIF-8 was exchanged with  $\text{Co}^{2+}$  through ion exchange, resulting in a Au-Co-MOF with Au and Co localized on MIL-125-NH<sub>2</sub> and ZIF-8, respectively. High-angle annular dark-field scanning transmission electron microscopy (HAADF-STEM) images and the corresponding energy dispersive X-ray spectroscopy (EDS) mapping show that Au clusters are located on MIL-125-NH<sub>2</sub> and the Co element is on ZIF-8 (Fig. S11). Control experiments confirmed that the Co element cannot be incorporated into MIL-125-NH<sub>2</sub> by the ion exchange process, ensuring its incorporation into ZIF-8 only (Table S1).

The obtained Au-Co-MOF composite with well-defined Au/Co locations is then converted into the corresponding oxide, namely **Au-Co-ZTO**, with the above two-step thermal treatment procedure as that for **ZTO-65**. Electron microscopy observation and powder XRD results indicate that the crystallinity and morphology of **Au-Co-ZTO** are similar to those of **ZTO-65** (Fig. 1b, S12 and S13). X-ray photoelectron spectroscopy (XPS)

reveals that Au is in its metallic state, while Co exhibits a mixed oxidation state of +2 and +3, identified as  $\text{CoO}_x$  (Fig. S14).<sup>40</sup> Furthermore, the Au clusters are hardly observed, indicating their tiny sizes, and primarily located on the central  $\text{TiO}_x$  based on EDS mapping results, whereas  $\text{CoO}_x$  species are predominantly distributed on the peripheral ZnO (Fig. S15, 1c and d). For comparison, **ZTO-65** with randomly distributed cocatalysts, referred to as **Au+Co+ZTO**, was also obtained by random impregnation of Au and Co species into **ZTO-65** (Fig. S16 and S17).

### Photocatalytic performance for methane oxidation

Encouraged by the above engineered interface coverage and precise cocatalyst placement, photocatalytic methane oxidation, which enables the conversion of  $\text{CH}_4$  into value-added oxygenates, has been conducted to investigate the significance of such structural design.<sup>41–45</sup> The experiment was investigated using  $\text{O}_2$  as the oxidizing agent and  $\text{H}_2\text{O}$  as the solvent. While the single-component ZIF-8-derived ZnO catalyst demonstrates the ability to selectively convert  $\text{CH}_4$  into liquid oxygenates, including  $\text{CH}_3\text{OH}$ ,  $\text{CH}_3\text{OOH}$ ,  $\text{HCHO}$ , and  $\text{HCOOH}$ , it gives very low activity (Table 1, entry 1; Fig. S18 and S19). In contrast, MIL-125-NH<sub>2</sub>-derived  $\text{TiO}_2$  shows higher activity than the above ZIF-8-derived ZnO; however, it readily generates over-oxidized  $\text{CH}_4$  to  $\text{CO}_2$ , resulting in low selectivity toward liquid oxygenate production (Table 1, entry 2).

Based on the high activity of MIL-125-NH<sub>2</sub>-derived  $\text{TiO}_2$  and high selectivity of ZIF-8-derived ZnO, it is assumed that **ZTO-*m*** composites could combine their respective advantages. Compared to their single-component counterparts, **ZTO-21** presents slightly increased activity for liquid oxygenate production with high selectivity, highlighting the importance of the heterojunction in promoting  $\text{CH}_4$  oxidation (Table 1, entry 3). Furthermore, as the coverage increases, the photocatalytic activity improves in the order of **ZTO-65** > **ZTO-35** > **ZTO-21** (Table 1, entry 3–5). Among these composites, **ZTO-65** shows the best performance, achieving an activity of  $628.7 \mu\text{mol g}^{-1} \text{h}^{-1}$ , which is 1.9 times higher than that of ZIF-8-derived ZnO and 1.4 times higher than that of MIL-125-NH<sub>2</sub>-derived  $\text{TiO}_2$ . Notably,

Table 1 Performance of photocatalytic methane oxidation over different catalysts derived from MOFs<sup>a</sup>

| Entry | Catalyst  | Yield ( $\mu\text{mol g}^{-1} \text{h}^{-1}$ ) |                        |                         |       |       | Liquid products | Liquid product selectivity |
|-------|---|--|------------------------|-------------------------|-------|-------|-----------------|----------------------------|
|       |   | $\text{CO}_2$                                  | $\text{CH}_3\text{OH}$ | $\text{CH}_3\text{OOH}$ | HCHO  | HCOOH |                 |                            |
| 1     | ZIF-8-derived ZnO                               | 0  | 51.2                   | 168.9                   | 96.4  | 13.2  | 329.7           | 1.00                       |
| 2     | MIL-125-NH <sub>2</sub> -derived $\text{TiO}_2$ | 152.3  | 95.4                   | 15.6                    | 325.0 | 14.8  | 450.8           | 0.75                       |
| 3     | <b>ZTO-21</b>                                   | 9.0  | 363.8                  | 25.7                    | 82.7  | 3.9   | 476.1           | 0.98                       |
| 4     | <b>ZTO-35</b>                                   | 3.7  | 128.6                  | 176.7                   | 248.0 | 7.8   | 561.1           | 0.99                       |
| 5     | <b>ZTO-65</b>                                   | 0  | 58.9                   | 391.5                   | 163.6 | 14.7  | 628.7           | 1.00                       |
| 6     | Mixture of MOF-derived ZnO and $\text{TiO}_2$   | 40.0   | 26.0                   | 114.3                   | 167.9 | 11.7  | 319.9           | 0.89                       |
| 7     | <b>Au-Co-ZTO</b>                                | 18.9   | 145.5                  | 1195.2                  | 360.2 | 22.6  | 1723.5          | 0.99                       |
| 8     | <b>Au+Co+ZTO</b>                                | 41.3   | 421.4                  | 331.0                   | 295.2 | 35.9  | 1083.5          | 0.96                       |

<sup>a</sup> Reaction conditions: catalyst (5 mg),  $\text{O}_2$  (1 bar),  $\text{CH}_4$  (20 bar),  $\text{H}_2\text{O}$  (10 mL), 25 °C, 300 W Xe lamp (320–800 nm).



**ZTO-65** not only exhibits higher activity, but also gives 100% selectivity toward liquid oxygenate production. As a control, the physical mixture of the MOF-derived ZnO and TiO<sub>2</sub> shows much lower activity and selectivity than the heterojunction composites (Table 1, entry 6; Fig. S20). These results unambiguously underscore the critical role of interface coverage for selective CH<sub>4</sub> oxidation.

The above results reveal that the interface coverage within heterojunction photocatalysts can be engineered using highly designable MOF composites as precursors (see SI, Discussion S1), which significantly influences the photocatalytic performance in CH<sub>4</sub> oxidation. To further improve CH<sub>4</sub> oxidation activity, Au and CoO<sub>x</sub> cocatalysts have been further introduced. First, the photocatalytic performance of **ZTO-65** with selectively loaded Au clusters on the TiO<sub>x</sub> component has been evaluated. Along with increased loading of Au clusters, the photocatalytic activity follows a volcano-type trend (Fig. S21a). At the optimal Au loading of 0.58 wt%, the CoO<sub>x</sub> cocatalyst was further introduced into the ZnO component, which indicates a similar activity trend as observed with Au loading change (Fig. S21b). When the Au and Co loadings reach 0.58 wt% and 0.39 wt%, respectively, the resulting **Au-Co-ZTO** exhibits the highest activity, achieving a liquid oxygenate production rate of 1723.5 μmol g<sup>-1</sup> h<sup>-1</sup> with 99% selectivity (Table 1, entry 7). Compared with previous reports,<sup>40,46–48</sup> the excellent performance of the heterojunction system with oxygen as the oxidant is significant

(Table S2). In contrast, the **Au+Co+ZTO** catalyst, where Au and CoO<sub>x</sub> cocatalysts are randomly distributed, showcases significantly lower activity than **Au-Co-ZTO**, highlighting the significance of precisely loaded and placed cocatalysts for enhanced CH<sub>4</sub> oxidation (Table 1, entry 8).

Furthermore, an isotope labeling experiment has been conducted to trace the source of liquid oxygenate production (Fig. 2a). When pure <sup>12</sup>CH<sub>4</sub> is used as the feedstock, two distinct single peaks are observed at 3.18 ppm and 3.68 ppm in the <sup>1</sup>H-nuclear magnetic resonance (<sup>1</sup>H-NMR) spectrum, corresponding to <sup>12</sup>CH<sub>3</sub>OH and <sup>12</sup>CH<sub>3</sub>OOH. In contrast, when a mixed gas of <sup>13</sup>CH<sub>4</sub>:<sup>12</sup>CH<sub>4</sub> in a 1:2 ratio is employed to replace pure <sup>12</sup>CH<sub>4</sub>, two split peaks appear due to the coupling splitting caused by the presence of <sup>13</sup>C.<sup>49</sup> Additionally, the ratio of <sup>13</sup>CH<sub>3</sub>OH/<sup>12</sup>CH<sub>3</sub>OH is 1:2, consistent with the ratio of feeding gases. These results clearly confirm that the liquid oxygenate production originates from CH<sub>4</sub>, rather than the decomposition of residual carbon. The stability of **Au-Co-ZTO** during photocatalysis has also been examined. After 5 consecutive photocatalytic cycles, no significant changes are observed in both activity and selectivity (Fig. 2b). Characterization confirms that the crystallinity and integrity are well preserved, suggesting the stability of the **Au-Co-ZTO** photocatalyst (Fig. S22–S25 and Table S3).

### Mechanism investigations

To unveil the mechanisms behind the enhanced photocatalytic performance of **Au-Co-ZTO**, charge transfer and CH<sub>4</sub> activation processes have been investigated. First, *in situ* XPS was employed to elucidate the charge transfer pathway in **ZTO-65**. Upon light irradiation, the Ti 2p binding energy shifts by -0.2 eV (Fig. 2c), whereas the Zn 2p binding energy increases by +0.2 eV (Fig. 2d). The results support that TiO<sub>x</sub> and ZnO form a heterojunction system, where electron transfer from ZnO to TiO<sub>x</sub> occurs, inferring that holes migrate from high oxidation potential TiO<sub>x</sub> to ZnO. Considering the relatively moderate oxidation capability of ZnO, the accumulation of holes in ZIF-8-derived ZnO mitigates the over-oxidation of CH<sub>4</sub> to CO<sub>2</sub> (Table 1, entry 1). The XPS analysis reveals that **ZTO-65** forms compact interfaces, which are more favorable for charge transfer compared with MOF-derived ZnO and TiO<sub>2</sub> (Fig. S26).

Additionally, the large interface areas within this heterojunction structure facilitate charge separation, contributing to the enhanced photocatalysis. All **ZTO-*m*** samples display similar light absorption properties, confirming that the differences in photocatalytic activity are not due to variations in light harvesting (Fig. S27). Steady-state photoluminescence (PL) spectroscopy reveals that **ZTO-65** exhibits the weakest fluorescence intensity (Fig. S28), suggesting the most efficient electron-hole separation among **ZTO-*m***. Similarly, photocurrent measurements and EIS also suggest that **ZTO-65** possesses the best charge separation efficiency and the lowest interface charge transfer resistance (Fig. S29 and S30). Furthermore, time-resolved transient photoluminescence reveals that **ZTO-65** has the longest electron lifetime (0.35 ns), followed by **ZTO-35** (0.30 ns) and **ZTO-21** (0.29 ns) (Fig. S31 and S32). The above results collectively demonstrate that the superior photocatalytic

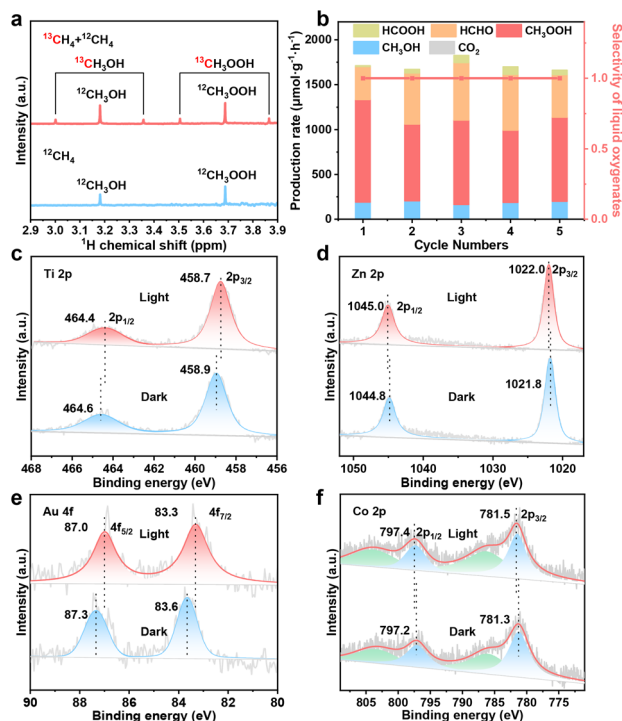


Fig. 2 (a) <sup>1</sup>H NMR spectra of the CH<sub>4</sub> oxidation reaction carried out with a <sup>13</sup>CH<sub>4</sub> and <sup>12</sup>CH<sub>4</sub> mixture (33.3% <sup>13</sup>CH<sub>4</sub> and 66.7% <sup>12</sup>CH<sub>4</sub>). (b) Recycling performance of **Au-Co-ZTO**. *In situ* XPS spectra for (c) Ti 2p, (d) Zn 2p of **ZTO-65** and (e) Au 4f of the sample obtained by thermal treatment of Au/MIL-125-NH<sub>2</sub>, as well as (f) Co 2p of **Au-Co-ZTO** in the dark and under light irradiation.



performance in **ZTO-65** arises from its large interface coverage in the heterojunction structure, which greatly enhances separation of electrons and holes, thereby benefiting the photocatalysis.

Moreover, the importance of precise cocatalyst placement in promoting charge separation has been investigated. Due to the overlap between Au 4f and Zn 3p XPS signals,<sup>45</sup> the sample directly from Au/MIL-125-NH<sub>2</sub> (similar thermal treatment to that for preparing **Au-Co-ZTO**) was employed instead to study the electronic state changes of Au under light irradiation. *In situ* XPS spectra reveal that, under light irradiation, the Au and Co peaks shift by  $-0.3$  eV and  $+0.2$  eV, respectively, indicating that Au clusters and CoO<sub>x</sub> function as reduction and oxidation cocatalysts, respectively (Fig. 2e and f). Therefore, the electron reduction reaction occurs on Au, while the hole oxidation reaction takes place on CoO<sub>x</sub> (Fig. S33).<sup>50</sup> In the heterojunction system, the spatial location of Au and CoO<sub>x</sub> would greatly impact charge separation efficiency. All steady-state PL, photocurrent, and EIS measurements confirm that **Au-Co-ZTO** exhibits superior charge separation efficiency compared to **Au+Co+ZTO** with Au and CoO<sub>x</sub> randomly distributed (Fig. S34). Time-resolved transient PL spectroscopy further indicates that **Au-Co-ZTO** has a longer fluorescence lifetime than **ZTO-m** without cocatalysts and **Au+Co+ZTO** (Fig. S35 and S36). These observations support that the precise cocatalyst placement is critical for promoting charge separation in heterojunction photocatalysts.

In addition to charge separation, the CH<sub>4</sub> activation process also plays a key role in photocatalytic CH<sub>4</sub> oxidation. The oxygen source for liquid oxygenate production was determined to elucidate the reaction pathway. With **Au-Co-ZTO** as the catalyst, mass spectrometry (MS) analysis of the liquid oxygenate

production gives the CH<sub>3</sub>OH signal only, as CH<sub>3</sub>OOH is unstable under the testing conditions.<sup>51</sup> The signals of CH<sub>3</sub><sup>18</sup>OH and CH<sub>3</sub><sup>16</sup>OH can be observed when <sup>18</sup>O<sub>2</sub> and H<sub>2</sub><sup>16</sup>O are used (Fig. 3a), suggesting that the oxygen in the products originates from both water and oxygen.

Furthermore, electron paramagnetic resonance (EPR) spectroscopy was employed to identify the reactive oxygen species (ROS) involved in the photocatalytic process. To identify signals originating from oxidation reactions, the catalysts were dispersed in water, and AgNO<sub>3</sub> was added to suppress interference from reduction-related ROS, such as <sup>•</sup>OOH.<sup>52</sup> No signal is detected in the dark when DMPO is used as the radical trapping agent (Fig. 3b). Upon light irradiation, DMPO-<sup>•</sup>OH signals are observed in the presence of **Au-Co-ZTO**, indicating the production of hydroxyl radicals (<sup>•</sup>OH) derived from H<sub>2</sub>O oxidation.<sup>52</sup> Similarly, the catalysts were dispersed in methanol (as a hole sacrificial agent) to investigate the ROS produced from reduction reactions. In this case, only DMPO-<sup>•</sup>OOH signals are detected, while <sup>•</sup>OH signals are absent (Fig. 3c). The DMPO-<sup>•</sup>OOH signals suggest that O<sub>2</sub> reacts with an electron and H<sup>+</sup> to form hydroperoxyl radical (<sup>•</sup>OOH) species, which are milder ROS than superoxide anions (O<sub>2</sub><sup>•-</sup>).<sup>53</sup> These EPR results demonstrate the formation of <sup>•</sup>OH and <sup>•</sup>OOH, where the former is produced from water oxidation by holes, while the latter results from the reduction of O<sub>2</sub> by electrons.

To further elucidate the roles of <sup>•</sup>OH and <sup>•</sup>OOH, quenching experiments were conducted (Fig. S37). The addition of salicylic acid, a <sup>•</sup>OH scavenger, significantly suppresses product formation, indicating that CH<sub>4</sub> activation is primarily driven by <sup>•</sup>OH. When Na<sub>2</sub>C<sub>2</sub>O<sub>4</sub>, the hole scavenger, is added, the activity decreases but is not completely suppressed. Introducing H<sub>2</sub>O<sub>2</sub> partially restores the activity, suggesting that water oxidation might not be the sole pathway for the <sup>•</sup>OH production. A smaller portion is generated from the decomposition of H<sub>2</sub>O<sub>2</sub>, which is produced from the further conversion of partial <sup>•</sup>OOH.<sup>54</sup> Unfortunately, <sup>•</sup>OH from H<sub>2</sub>O<sub>2</sub> is hardly detected by EPR due to its low concentration.<sup>55</sup>

According to these results, a potential photocatalytic CH<sub>4</sub> oxidation mechanism is proposed (Fig. 3d). During photocatalysis, photogenerated holes oxidize H<sub>2</sub>O to produce <sup>•</sup>OH, while electrons reduce O<sub>2</sub> to form <sup>•</sup>OOH. A fraction of <sup>•</sup>OOH undergoes hydrogenation to yield H<sub>2</sub>O<sub>2</sub>, which subsequently decomposes to release additional <sup>•</sup>OH.<sup>56</sup> The generated <sup>•</sup>OH abstracts a hydrogen atom from CH<sub>4</sub>, forming methyl radicals (<sup>•</sup>CH<sub>3</sub>) and initiating the methane activation (step I).<sup>57</sup> The <sup>•</sup>CH<sub>3</sub> radicals then react with <sup>•</sup>OOH to produce CH<sub>3</sub>OOH, which undergoes further transformation to CH<sub>3</sub>OH (step II, III). In addition, CH<sub>3</sub>OH also can be formed through the direct reaction between <sup>•</sup>OH and <sup>•</sup>CH<sub>3</sub> (step IV).<sup>57</sup> Dehydration of CH<sub>3</sub>OOH or further oxidation of CH<sub>3</sub>OH results in HCHO, which can be subsequently oxidized to HCOOH and eventually CO<sub>2</sub> (step V-VIII).

Based on the reaction mechanism, the production rates of <sup>•</sup>OH and <sup>•</sup>OOH were quantified to unveil the influence of cocatalyst placement on surface reactions. EPR spectra show similar ROS production over **Au+Co+ZTO** and **Au-Co-ZTO**, indicating that the reaction pathway is undisturbed by the

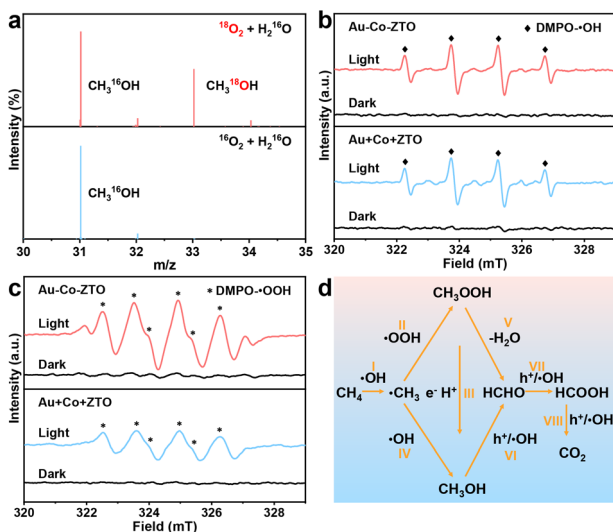


Fig. 3 (a) MS results of the isotope labeling experiments in the presence of <sup>18</sup>O<sub>2</sub> + H<sub>2</sub><sup>16</sup>O or <sup>16</sup>O<sub>2</sub> + H<sub>2</sub><sup>16</sup>O over **Au-Co-ZTO**. EPR spectra of (b) DMPO-<sup>•</sup>OH and (c) DMPO-<sup>•</sup>OOH for monitoring the generation of <sup>•</sup>OH and <sup>•</sup>OOH active species over **Au-Co-ZTO** and **Au+Co+ZTO**. (d) Schematic illustration of the mechanism of photocatalytic CH<sub>4</sub> conversion.



cocatalyst placement (Fig. 3b and c). However, while the DMPO- $\cdot\text{OH}$  signal intensity is comparable, the DMPO- $\cdot\text{OOH}$  intensity is obviously weaker for **Au+Co+ZTO** than **Au-Co-ZTO**. This suggests that the cocatalyst placement significantly impacts the oxygen reduction to  $\cdot\text{OOH}$  but has a minimal impact on  $\text{H}_2\text{O}$  oxidation to  $\cdot\text{OH}$ , which avoids over-oxidation of liquid oxygenate production by excess  $\cdot\text{OH}$ . Furthermore, the production rate of different ROS was quantified by probe experiments for the two catalysts. Specifically, coumarin acted as the fluorescence probe for  $\cdot\text{OH}$  detection, and the degradation rate of nitrotetrazolium blue chloride (NBT) was adopted to examine  $\cdot\text{OOH}$ .<sup>43</sup> The PL intensity growth rate of 7-hydroxycoumarin originating from the reaction between coumarin and  $\cdot\text{OH}$  is nearly equal, supporting that the placement of cocatalysts does not affect the water oxidation to  $\cdot\text{OH}$  (Fig. 4a and S38). However, the NBT degradation rate, indicative of  $\cdot\text{OOH}$  production, is higher for **Au-Co-ZTO**, consistent with the EPR results (Fig. 4b and S39). These findings demonstrate that the cocatalyst placement not only improves the charge separation, but also accelerates the  $\text{O}_2$  activation to  $\cdot\text{OOH}$  for boosting photocatalytic activity.

In addition, mechanisms regarding how the cocatalyst placement influences  $\text{CH}_4$  activation have been investigated. XPS analysis was employed to disclose the electronic states of Au and Co, which affect the activation of intermediates. The Au 4f<sub>7/2</sub> signal for **Au+Co+ZTO** appears at 83.5 eV, while it shifts to 83.3 eV for **Au-Co-ZTO**, indicating an increased electronic density of Au in the latter (Fig. 4c). This increased electronic density of Au clusters in **Au-Co-ZTO** enables efficient electron donation to  $\text{O}_2$ , thereby facilitating activation of  $\text{O}_2$ .<sup>58</sup> In contrast, no difference is observed in the Co XPS signals between the two catalysts (Fig. 4d). This indicates that the absorption and activation of  $\text{H}_2\text{O}$  on  $\text{CoO}_x$  are comparable,

consistent with their similar abilities to produce  $\cdot\text{OH}$  from water oxidation (Fig. 3b and 4a). These results suggest that the cocatalyst distribution modulates the electronic states of Au, further enhancing  $\text{O}_2$  activation for improved  $\text{CH}_4$  oxidation.

## Conclusions

In summary, heterojunction photocatalysts with engineered surface coverage and precise cocatalyst placement have been fabricated by pre-assembly of binary MOF composites, followed by two-step thermal treatment. ZnO coverage on the  $\text{TiO}_x$  surface in the heterojunction composites is systematically regulated by varying the interface coverage between their respective MOF precursors, resulting in **ZTO-*m*** ( $m = 21, 35, 65$ ), for photocatalytic  $\text{CH}_4$  oxidation. It is observed that **ZTO-65** with the largest interface coverage between the two components significantly improves charge separation and displays the highest activity with 100% selectivity toward liquid oxygenate production, disclosing the critical role of interface coverage in photocatalysis.

On the basis of **ZTO-65** with optimized interface coverage, the cocatalysts, Au clusters and  $\text{CoO}_x$ , are further deposited on  $\text{TiO}_x$  and ZnO, respectively. The spatial distribution of cocatalysts is found to affect charge separation, and meanwhile, improve  $\text{O}_2$  activation, further optimizing the performance for photocatalytic  $\text{CH}_4$  oxidation. Accordingly, the optimized **Au-Co-ZTO** achieves a liquid oxygenate production yield of 1723.5  $\mu\text{mol g}^{-1} \text{h}^{-1}$  with an impressive selectivity of 99%. This work not only highlights the great potential of MOFs toward photocatalysis, but also offers deep insights into the development of heterostructured photocatalytic materials.

## Author contributions

H.-L. J. and Q. C. supervised the project. W. Z., K. S. and J. X. performed all synthetic and characterization experiments. Z. L. assisted in figures. M. H. provided valuable discussions. W. Z., K. S. and H.-L. J. co-wrote the manuscript. All authors discussed the results and commented on the manuscript.

## Conflicts of interest

There are no conflicts to declare.

## Data availability

The additional figures, tables, and data supporting this article have been included as part of the SI. Supplementary information is available. See DOI: <https://doi.org/10.1039/d5sc04771d>.

## Acknowledgements

This work was supported by the National Key Research and Development Program of China (2021YFA1500400), the National Natural Science Foundation of China (22331009, 22405259, and W2512006), the Strategic Priority Research Program of the Chinese Academy of Sciences (XDB0450302), the

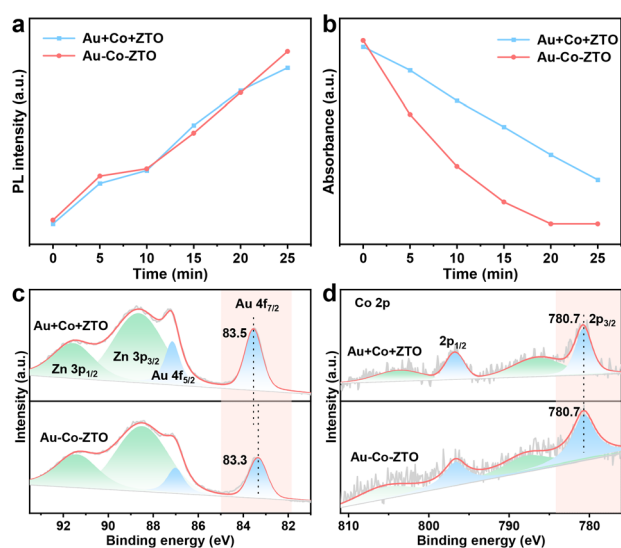


Fig. 4 (a) Time-dependent PL intensity of the produced 7-hydroxycoumarin for  $\cdot\text{OH}$  radical detection. (b) Time-dependent absorption intensity of NBT for  $\cdot\text{OOH}$  radical detection. XPS spectra for (c) Au 4f and (d) Co 2p of **Au-Co-ZTO** and **Au+Co+ZTO**.



International Partnership Program of CAS (123GJHZ2022028MI), and the China Postdoctoral Science Foundation (BX20230348, 2023M743374). This work was partially carried out at the Instruments Center for Physical Science, USTC.

## References

- 1 S. Shoji, X. Peng, A. Yamaguchi, R. Watanabe, C. Fukuhara, Y. Cho, T. Yamamoto, S. Matsumura, M.-W. Yu, S. Ishii, T. Fujita, H. Abe and M. Miyauchi, *Nat. Catal.*, 2020, **3**, 148–153.
- 2 Y. Yuan, L. Zhou, H. Robotjazi, J. L. Bao, J. Zhou, A. Bayles, L. Yuan, M. Lou, M. Lou, S. Khatiwada, E. A. Carter, P. Nordlander and N. J. Halas, *Science*, 2022, **378**, 889–893.
- 3 K. Sun, Y. Huang, F. Sun, Q. Wang, Y. Zhou, J. Wang, Q. Zhang, X. Zheng, F. Fan, Y. Luo, J. Jiang and H.-L. Jiang, *Nat. Chem.*, 2024, **16**, 1638–1646.
- 4 F. Chen, T. Ma, T. Zhang, Y. Zhang and H. Huang, *Adv. Mater.*, 2021, **33**, 2005256.
- 5 L. Zhang, J. Liu and Y.-Q. Lan, *Acc. Chem. Res.*, 2024, **57**, 870–883.
- 6 S. Bhattacharjee, S. Linley and E. Reisner, *Nat. Rev. Chem.*, 2024, **8**, 87–105.
- 7 R. S. H. Khoo, C. Fiankor, S. Yang, W. Hu, C. Yang, J. Lu, M. D. Morton, X. Zhang, Y. Liu, J. Huang and J. Zhang, *J. Am. Chem. Soc.*, 2023, **145**, 24052–24060.
- 8 B. Zhu, J. Sun, Y. Zhao, L. Zhang and J. Yu, *Adv. Mater.*, 2024, **36**, 2310600.
- 9 A. Dhakshinamoorthy, Z. Li, S. Yang and H. Garcia, *Chem. Soc. Rev.*, 2024, **53**, 3002–3035.
- 10 J. Yang, D. Wang, H. Han and C. Li, *Acc. Chem. Res.*, 2013, **46**, 1900–1909.
- 11 Q. Zhang, C. Yang, Y. Chen, Y. Yan, M. Kan, H. Wang, X. Lv, Q. Han and G. Zheng, *Angew. Chem., Int. Ed.*, 2025, **64**, e202419282.
- 12 A. V. Akimov, A. J. Neukirch and O. V. Prezhdo, *Chem. Rev.*, 2013, **113**, 4496–4565.
- 13 P. Wang, C. Jia, Y. Huang and X. Duan, *Matter*, 2021, **4**, 552–581.
- 14 B. Qiu, M. Du, Y. Ma, Q. Zhu, M. Xing and J. Zhang, *Energy Environ. Sci.*, 2021, **14**, 5260–5288.
- 15 Y. Qi, J. Zhang, Y. Kong, Y. Zhao, S. Chen, D. Li, W. Liu, Y. Chen, T. Xie, J. Cui, C. Li, K. Domen and F. Zhang, *Nat. Commun.*, 2022, **13**, 484.
- 16 M.-Y. Qi, Y.-H. Li, F. Zhang, Z.-R. Tang, Y. Xiong and Y.-J. Xu, *ACS Catal.*, 2020, **10**, 3194–3202.
- 17 H. Furukawa, K. E. Cordova, M. O’Keeffe and O. M. Yaghi, *Science*, 2013, **341**, 1230444.
- 18 H.-C. J. Zhou and S. Kitagawa, *Chem. Soc. Rev.*, 2014, **43**, 5415–5418.
- 19 Y. Shen, T. Pan, L. Wang, Z. Ren, W. Zhang and F. Huo, *Adv. Mater.*, 2021, **33**, 2007442.
- 20 X. Zhao, Y. Wang, D.-S. Li, X. Bu and P. Feng, *Adv. Mater.*, 2018, **30**, 1705189.
- 21 Q.-J. Wu, J. Liang, Y.-B. Huang and R. Cao, *Acc. Chem. Res.*, 2022, **55**, 2978–2997.
- 22 T. Zhang and W. Lin, *Chem. Soc. Rev.*, 2014, **43**, 5982–5993.
- 23 G. Li, S. Zhao, Y. Zhang and Z. Tang, *Adv. Mater.*, 2018, **30**, 1800702.
- 24 J. Liu, T. A. Goetjen, Q. Wang, J. G. Knapp, M. C. Wasson, Y. Yang, Z. H. Syed, M. Delferro, J. M. Notestein, O. K. Farha and J. T. Hupp, *Chem. Soc. Rev.*, 2022, **51**, 1045–1097.
- 25 L. Jiao, J. Wang and H.-L. Jiang, *Acc. Mater. Res.*, 2021, **2**, 327–339.
- 26 R.-B. Lin, Z. Zhang and B. Chen, *Acc. Chem. Res.*, 2021, **54**, 3362–3376.
- 27 Y.-Z. Chen, R. Zhang, L. Jiao and H.-L. Jiang, *Coord. Chem. Rev.*, 2018, **362**, 1–23.
- 28 K. J. Lee, J. H. Lee, S. Jeoung and H. R. Moon, *Acc. Chem. Res.*, 2017, **50**, 2684–2692.
- 29 Y.-T. Zheng, S. Li, N.-Y. Huang, X. Li and Q. Xu, *Coord. Chem. Rev.*, 2024, **510**, 215858.
- 30 T. De Villenoisy, X. Zheng, V. Wong, S. S. Mofarah, H. Arandiyani, Y. Yamauchi, P. Koshy and C. C. Sorrell, *Adv. Mater.*, 2023, **35**, 2210166.
- 31 L. Chai, R. Li, Y. Sun, K. Zhou and J. Pan, *Adv. Mater.*, 2025, **37**, 2413658.
- 32 C. Wang, Y. Yao, J. Li and Y. Yamauchi, *Acc. Mater. Res.*, 2022, **3**, 426–438.
- 33 G. Cai, P. Yan, L. Zhang, H.-C. Zhou and H.-L. Jiang, *Chem. Rev.*, 2021, **121**, 12278–12326.
- 34 C. Liu, T. Bao, L. Yuan, C. Zhang, J. Wang, J. Wan and C. Yu, *Adv. Funct. Mater.*, 2022, **32**, 2111404.
- 35 S. Park, D. Oh, J. Ahn, J. K. Kim, D.-H. Kim, S. Kim, C. Park, W. Jung and I.-D. Kim, *Adv. Mater.*, 2022, **34**, 2201109.
- 36 C. Chuaicham, S. Karthikeyan, J. T. Song, T. Ishihara, B. Ohtani and K. Sasaki, *ACS Appl. Mater. Interfaces*, 2020, **12**, 9169–9180.
- 37 K. S. Ranjith and T. Uyar, *CrystEngComm*, 2018, **20**, 5801–5813.
- 38 F. Cao, Y. Zhang, H. Wang, K. Khan, A. K. Tareen, W. Qian, H. Zhang and H. Ågren, *Adv. Mater.*, 2022, **34**, 2107554.
- 39 Y.-C. Liang, C.-Y. Hu and Y.-C. Liang, *CrystEngComm*, 2012, **14**, 5579–5584.
- 40 H. Song, X. Meng, S. Wang, W. Zhou, S. Song, T. Kako and J. Ye, *ACS Catal.*, 2020, **10**, 14318–14326.
- 41 B. An, Z. Li, Z. Wang, X. Zeng, X. Han, Y. Cheng, A. M. Sheveleva, Z. Zhang, F. Tuna, E. J. L. McInnes, M. D. Frogley, A. J. Ramirez-Cuesta, L. S. Natrajan, C. Wang, W. Lin, S. Yang and M. Schröder, *Nat. Mater.*, 2022, **21**, 932–938.
- 42 C. Feng, S. Zuo, M. Hu, Y. Ren, L. Xia, J. Luo, C. Zou, S. Wang, Y. Zhu, M. Rueping, Y. Han and H. Zhang, *Nat. Commun.*, 2024, **15**, 9088.
- 43 L. Luo, Z. Gong, Y. Xu, J. Ma, H. Liu, J. Xing and J. Tang, *J. Am. Chem. Soc.*, 2022, **144**, 740–750.
- 44 S. Song, H. Song, L. Li, S. Wang, W. Chu, K. Peng, X. Meng, Q. Wang, B. Deng, Q. Liu, Z. Wang, Y. Weng, H. Hu, H. Lin, T. Kako and J. Ye, *Nat. Catal.*, 2021, **4**, 1032–1042.
- 45 P. Wang, R. Shi, Y. Zhao, Z. Li, J. Zhao, J. Zhao, G. I. N. Waterhouse, L.-Z. Wu and T. Zhang, *Angew. Chem., Int. Ed.*, 2023, **62**, e202304301.



- 46 Y. Jiang, W. Zhao, S. Li, S. Wang, Y. Fan, F. Wang, X. Qiu, Y. Zhu, Y. Zhang, C. Long and Z. Tang, *J. Am. Chem. Soc.*, 2022, **144**, 15977–15987.
- 47 X. Sun, X. Chen, C. Fu, Q. Yu, X.-S. Zheng, F. Fang, Y. Liu, J. Zhu, W. Zhang and W. Huang, *Nat. Commun.*, 2022, **13**, 6677.
- 48 Y. Cao, W. Yu, Y. Li, J. Meng, K. Zheng, C. Huang, X. Yang, Y. Yang, F. Dong and Y. Zhou, *Adv. Energy Mater.*, 2025, **15**, 2404871.
- 49 V. Fernandes de Almeida, S. Navalón, A. Dhakshinamoorthy and H. Garcia, *Angew. Chem., Int. Ed.*, 2025, **64**, e202424537.
- 50 T. Zhou, J. Wang, S. Chen, J. Bai, J. Li, Y. Zhang, L. Li, L. Xia, M. Rahim, Q. Xu and B. Zhou, *Appl. Catal. B*, 2020, **267**, 118599.
- 51 Y. Jiang, S. Li, S. Wang, Y. Zhang, C. Long, J. Xie, X. Fan, W. Zhao, P. Xu, Y. Fan, C. Cui and Z. Tang, *J. Am. Chem. Soc.*, 2023, **145**, 2698–2707.
- 52 C. Xu, Y. Pan, G. Wan, H. Liu, L. Wang, H. Zhou, S.-H. Yu and H.-L. Jiang, *J. Am. Chem. Soc.*, 2019, **141**, 19110–19117.
- 53 J. Wang and S. Wang, *Chem. Eng. J.*, 2020, **401**, 126158.
- 54 Q. Zhang, K. Gu, C. Dong, C. Xue, H. Che, K. Zhang and Y. Ao, *Angew. Chem., Int. Ed.*, 2025, **64**, e202417591.
- 55 J.-N. Chang, Q. Li, J.-W. Shi, M. Zhang, L. Zhang, S. Li, Y. Chen, S.-L. Li and Y.-Q. Lan, *Angew. Chem., Int. Ed.*, 2023, **62**, e202218868.
- 56 Y. Nosaka and A. Y. Nosaka, *Chem. Rev.*, 2017, **117**, 11302–11336.
- 57 J. Sui, M.-L. Gao, B. Qian, C. Liu, Y. Pan, Z. Meng, D. Yuan and H.-L. Jiang, *Sci. Bull.*, 2023, **68**, 1886–1893.
- 58 W. Yang, F. Qi, W. An, H. Yu, S. Liu, P. Ma, R. Chen, S. Liu, L.-L. Lou and K. Yu, *ACS Catal.*, 2024, **14**, 5936–5948.

